Bayesian transdimensional inverse reconstruction of the ^{137}Cs Fukushima-Daiichi release

Joffrey Dumont Le Brazidec[1,2], Marc Bocquet[2], Olivier Saunier[1], and Yelva Roustan[2]

[1]IRSN, PSE-SANTE, SESUC, BMCA, Fontenay-aux-Roses, France
[2]CEREA, École des Ponts and EDF R&D, Île-de-France, France

Correspondence: Joffrey Dumont Le Brazidec (joffrey.dumont@enpc.fr)

Abstract.

The accident at the Fukushima-Daiichi nuclear power plant yielded massive and rapidly varying atmospheric radionuclide releases. The assessment of these releases and of the corresponding uncertainties can be performed using inverse modelling methods that combine an atmospheric transport model with a set of observations and have proven to be very effective for this type of problem. In the case of Fukushima-Daiichi, a Bayesian inversion is particularly suitable because it allows errors to be modelled rigorously and a large amount of observations of different natures to be assimilated at the same time. More specifically, one of the major sources of uncertainty in the source assessment of the Fukushima-Daiichi releases stems from the temporal representation of the source. To obtain a well time-resolved estimate, we implement a sampling algorithm within a Bayesian framework, the Reversible-Jump Markov Chain Monte Carlo, in order to retrieve the distributions of the magnitude of the Fukushima-Daiichi caesium 137 source as well as its temporal discretisation. In addition, we develop Bayesian methods allowing to combine air concentration and deposition measurements, as well as to assess the spatio-temporal information of the air concentration observations in the definition of the observation error matrix.

These methods are applied to the reconstruction of the posterior distributions of the magnitude and temporal evolution of the caesium 137 release. They yield a source estimate between 11 and 24 March, as well as an assessment of the uncertainties associated with the observations, the model and the source estimate. The total released reconstructed activity is estimated to be between 10 and 20 PBq, although it increases when taking into account the deposition measurements. Finally, the variable discretisation of the source term yields an almost hourly profile over certain intervals of high temporal variability, signaling identifiable portions of the source term.

1 Introduction

1.1 Fukushima-Daiichi nuclear accident

On 11 March 2011, an earthquake under the Pacific Ocean off the coast of Japan triggered an extremely destructive tsunami that hit the Japanese coastline about an hour later, killing 18,000 people. These events led to the automatic shutdown of four Japanese nuclear power plants. However the drowning of emergency power generators prevented the cooling system to function, making the shutdown impossible at the Fukushima-Daiichi nuclear power plant (NPP). This yielded a massive release

1

of radionuclides characterised by several episodes of varying intensity, which lasted for several weeks. The estimation of such a release is difficult and subject to significant uncertainties. Reconstructing the temporal evolution of the caesium 137 (^{137}Cs) source means to find a highly variable release rate running over several hundreds of hours.

Since 2011, several approaches have been proposed to assess the Fukushima-Daiichi radionuclide release source terms. For instance, methods based on the simple comparison between observations and simulated predictions have been investigated by Chino et al. (2011); Katata et al. (2012); Mathieu et al. (2012); Terada et al. (2012); Hirao et al. (2013); Kobayashi et al. (2013); Katata et al. (2015); Nagai et al. (2017). Ambitious inverse problem methods have been developed by, e.g., Stohl et al. (2012); Yumimoto et al. (2016); Li et al. (2019). In particular, Winiarek et al. (2012, 2014) used air concentration and deposition measurements to assess the source term of ^{137}Cs by rigorously estimating the errors; Saunier et al. (2013) evaluated the source term by inverse modelling with ambient gamma dose measurements. Finally, inverse problem methods based on a full Bayesian formalism have also been used. Liu et al. (2017) apply several methods including MCMC algorithms to estimate the time evolution of the ^{137}Cs release, accompanied by an estimate of the associated uncertainty. Terada et al. (2020) refined the ^{137}Cs source term with an optimisation method based on a Bayesian inference from several measurement databases.

1.2 Bayesian inverse modelling and sampling of a radionuclide source

Bayesian inverse problem methods have been shown to be effective in estimating radionuclide sources (Delle Monache et al., 2008; Tichý et al., 2016; Liu et al., 2017). Here, we briefly describe this Bayesian framework for source term reconstruction; a more complete description is available in Dumont Le Brazidec et al. (2021). The crucial elements defining the control variable vector of the source $\boldsymbol{x}$ are i) $\ln \boldsymbol{q}$, a vector whose components correspond to the logarithm of the release rates q_i (constant releases on a time interval, such as a day or an hour), and ii) hyperparameters such as entries of the observation error scale matrix $\mathbf{R}$ or the time windows of the release rates (more details in section 3).

The posterior probability density function (pdf) of $\boldsymbol{x}$ is given by Bayes' rule:

$$p(\boldsymbol{x}|\boldsymbol{y}) = \frac{p(\boldsymbol{y}|\boldsymbol{x})p(\boldsymbol{x})}{p(\boldsymbol{y})} \propto p(\boldsymbol{y}|\boldsymbol{x})p(\boldsymbol{x}) \tag{1}$$

with $\boldsymbol{y}$ the observation vector. The pdf $p(\boldsymbol{y}|\boldsymbol{x})$ is the likelihood, which quantifies the fit of the source vector $\boldsymbol{x}$ to the data. More precisely, the observations $\boldsymbol{y}$ are compared to a set of modelled concentrations: $\mathbf{H}\boldsymbol{q}$, i.e., the predictions, constructed using a numerical simulation of the radionuclide transport from the source. $\mathbf{H}$ is the observation operator, the matrix representing the integration in time (i.e. resolvent) of the atmospheric transport model. Therefore, the predictions of the model are considered linear in $\boldsymbol{q}$. The likelihood is often chosen as a distribution parametrised with an observation error scale matrix $\mathbf{R}$. The pdf $p(\boldsymbol{x})$ represents the information available on the source before data assimilation.

Once the likelihood and the prior are defined, the posterior distribution can be estimated using a sampling algorithm. Sampling techniques include in particular the very popular Markov chain Monte Carlo (MCMC) methods that assess the posterior pdf of the source, or marginal pdfs thereof. It has been applied by Delle Monache et al. (2008) to estimate the Algeciras incident source location, by Keats et al. (2007), or Yee et al. (2014) who evaluated Xenon-133 releases at Chalk River Laboratories.

More recently, the technique was used to assess the uncertainties of the source reconstruction by Liu et al. (2017); Dumont Le Brazidec et al. (2020, 2021).

1.3 Transdimensional analysis and objectives of this study

60 The problem of finding a proper representation of x, i.e. a discretisation of the source term, is the problem of finding the adequate step function for q, i.e., the optimal number of steps, the optimal time length of each step and the corresponding release rates. This representation depends on the case under study: depending on the observations, more or less information is available to define a more or less resolved in time source term. In other words, depending on the data available to inform about the source term, the steps of the function supporting q could be small (a lot of available information allowing for a fine

65 representation) or large (few information available bringing a coarse representation), yielding an irregular discretisation in time of the source term. Note that the choice of the discretisation can be seen as a balancing issue due to the bias-variance trade-off principle (Hastie et al., 2009): low complexity models are prone to high bias but low variance, while high complexity models are prone to low bias but high variance. The difficulty in the source term discretisation is that of selecting representations that are sufficiently rich, but not too complex to avoid over-fitting that leads to high variance error and too much computing time.

70 Radionuclides releases such as those of ^{137}Cs from the Fukushima-Daiichi NPP are very significant over a long period of time (several weeks), and with a very high temporal variability. In such case, the choice of the discretisation is a crucial and challenging task.

In this paper we explore several ways to improve the source term assessment and its corresponding uncertainty. In the first instance, we address the issue of sampling in the case of massive and highly fluctuating releases of radionuclides to the

75 atmosphere. In the second instance, we propose several statistical models of the likelihood scale matrix depending on the available set of observations.

The outline of the paper is as follows. First, in section 2, the observations dataset used in this study is described as well as the physical model of the problem.

Second, in section 3, we describe the theoretical aspects of this study and first focus on the concepts of transdimensionality

80 and model selection. The Reversible-Jump MCMC algorithm (RJ-MCMC) used to shape the release rates vector q is presented in subsection 3.1. Then, other ways to improve the sampling quality and reduce uncertainties are explored through the addition of information in subsection 3.2. In particular, methods that combine deposition and concentrations observations or that exploit the temporal and spatial information of the observations in the definition of the likelihood scale matrix $\mathbf{R}$ are proposed.

Subsequently, these methods are evaluated in section 4. Specifically, once the statistical parametrisation of the problem is

85 chosen in subsection 4.1, the advantages of the RJ-MCMC are explored in subsection 4.2.1. The impact of using the deposition measurements and the use of the observation temporal and spatial information are described in subsections 4.2.2 and 4.2.3. We finally conclude on the contribution of each method.

This article is in line with the authors' earlier studies (Liu et al., 2017; Dumont Le Brazidec et al., 2020, 2021) and is inspired from the insightful work of Bodin and Sambridge (2009). In particular, the RJ-MCMC algorithm is applied by Liu

90 et al. (2017) on the Fukushima-Daiichi case with variable discretisations but with a fixed number of steps (i.e. grid cells).

3

Here, it is applied in a more ambitious transdimensional framework where the number of steps of the discretisation is modified through the progression of the RJ-MCMC, and using a significantly larger dataset.

2 Fukushima-Daiichi NPP ^{137}Cs release and numerical modelling

2.1 Observations dataset

95 The dataset used in this study consists of ^{137}Cs air concentration and deposition measurements over the Japanese territory. The vector of ^{137}Cs air concentration measurements contains $14,248$ observations (Furuta et al., 2011; Yamada et al., 2013; Oura et al., 2015; Nagakawa et al., 2015; Tanaka et al., 2013; Tsuruta et al., 2018; Takehisa et al., 2012) from 105 stations, whose locations are shown in Fig. 1. This dataset is significantly larger than the one used by Liu et al. (2017). It allows us to better
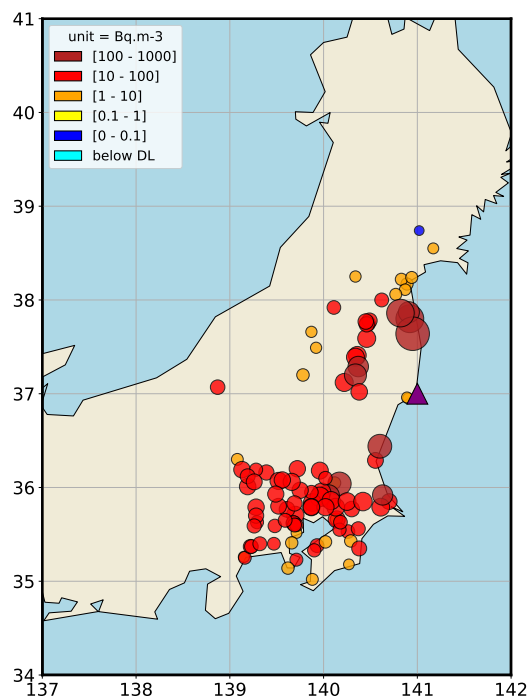

Figure 1. Maximum air concentrations of ^{137}Cs in Bq.m^{-3} measured in Japan in March 2011. The light blue points correspond to concentrations below the detection limit. The purple triangle corresponds to the Fukushima-Daiichi NPP.

evaluate the relevance of our methods and to accurately estimate the uncertainties of the problem. Moreover, the majority

100 of these observations are hourly, which allows for a fine sampling of the ^{137}Cs source term. Additionally, 1507 deposition measurements are used. This dataset is described and available in MEXT (2012). The observations are located within $300\,\mathrm{km}$ of the Fukushima-Daiichi NPP. However, measurements too close to the Fukushima-Daiichi plant (typically less than 5 times

the spatial resolution of the meteorological fields described in table 1 are not used to take into account the short-range dilution effects of the transport model. These measurements represent the averages of each grid cell of a field of deposition observations in $Bq.m^{-2}$ measured by aerial radiation monitoring.

2.2 Physical parametrisation

The atmospheric ^{137}Cs plume dispersion is simulated with the Eulerian model ldX, already validated on the Chernobyl and Fukushima-Daiichi accidents (Quélo et al., 2007; Saunier et al., 2013), or again on the ^{106}Ru releases in 2017 (Saunier et al., 2019; Dumont Le Brazidec et al., 2020, 2021). The meteorological data used are the three-hourly OPER OD ECMWF fields (see Table 1).

	ECMWF
Spatial resolution	$0.125° \times 0.125°$
Time resolution	3 hours
Vertical resolution	11 terrain following layers (from 0 to 4400 m)
Vertical mixing	K-diffusion parametrised with Louis' closure (Louis, 1979)
	and (Troen and Mahrt, 1986) in PBL unstable conditions
Horizontal mixing	constant horizontal eddy diffusion coefficient $K_h = 0\,\mathrm{m^2 s^{-1}}$
Wet scavenging	$\lambda = \Lambda_0 p_0$ (below-cloud) with $\Lambda_0 = 5.10^{-5}\,\mathrm{h.(mm.s)^{-1}}$, and $\lambda = \Lambda_1 p_0^{0.64}$ (in-cloud) with $\Lambda_1 = 5.10^{-4}\,\mathrm{h.(mm.s)^{-1}}$; and p_0 is the rainfall intensity (Baklanov and Sørensen, 2001; Querel et al., 2021)
Dry deposition	constant deposition velocity $v_d = 2.10^{-3}\,\mathrm{m.s^{-1}}$

Table 1. Main setup parametrisations of the ldX ^{137}Cs transport simulations. Spatial and time resolutions are those of the ECMWF meteorological fields and the transport model. The other entries correspond to parameters of the transport model only.

The radionuclides, and in particular ^{137}Cs, were mainly deposited in the Fukushima Prefecture, north-west of the Fukushima-Daiichi NPP. The bulk of the releases occurred over a two-week period from 11 March on. Therefore, the model simulations start on 11 March 2011 at 00:00 UTC and end on 24 March 2011, corresponding to 312 hours during which radionuclides could have been released. The release is assumed to be spread over the first two vertical layers of the model (between 0 and 160m). The height of the release has a small impact because the modelled predictions are compared with observations sufficiently far away from the Fukushima-Daiichi NPP and the release mostly remains within the atmospheric boundary layer. Finally, it is assumed that all parameters describing the source aside from the reconstructed ones are known. This is for instance the case of the release height.

3 Methodological aspects of the inverse problem

3.1 Reversible-Jump MCMC

In this section, we describe the Bayesian Reversible-Jump MCMC algorithm used in the following to reconstruct the vector $\mathbf{q}$ discretised over a variable adaptive grid. A good description of the RJ-MCMC, which was introduced by Green (1995), can be found in Hastie and Green (2012). The algorithm is also clearly explained and applied by Bodin and Sambridge (2009). The method was in particular used by Yee (2008) in the field of inverse modelling for the assessment of substance releases, and by Liu et al. (2017) to quantify Fukushima-Daiichi releases, but with a fixed number of variable size gridcells. A key asset of the RJ-MCMC technique is its ability to sample a highly variable release by balancing bias and variance errors.

The RJ-MCMC algorithm is a natural extension of the traditional Metropolis-Hastings (MH) algorithm but to transdimensional discretisation grids. In a traditional MH, the distribution of the release is assessed through a succession of random walks (e.g., Dumont Le Brazidec et al., 2020). In particular, special random walks allow the pdf of the discretisation steps within the control vector $\boldsymbol{x}$ to be sampled.

Indeed, as described above, the function that describes the evolution of the release rate over time is a vector or step function where each step (i.e., a gridcell) defines a constant release rate over a time interval. When using the RJ-MCMC, these time intervals are neither fixed nor regularly spaced. An objective is hence to retrieve the best step-wise time partition of the source term, which defines the release rates.

To do this, we use the concept of boundary: a boundary is a time that separates two constant release rates, i.e., that separates two gridcells where the source term is defined. Let Λ be the set of N_b boundaries. Boundaries are 0, 312, and integers in
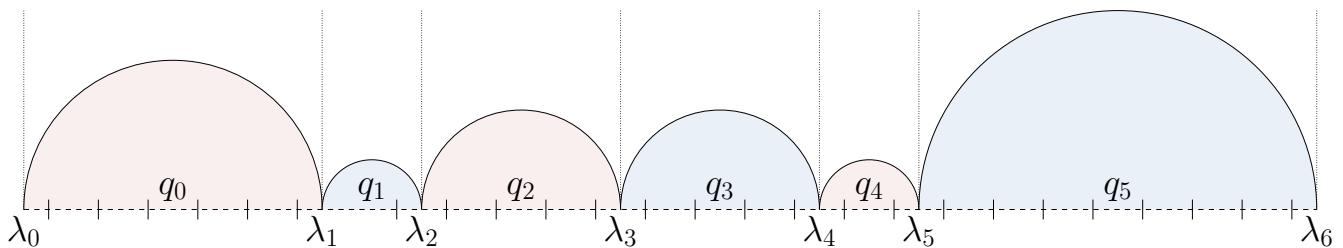

Figure 2. Example of a source term partition: $\Lambda = (\lambda_0, \dots, \lambda_6)$ is the set of boundaries and $\boldsymbol{q} = (q_0, \dots, q_5)$ is the vector of release rates. The release rate defined on the time interval $[\lambda_2, \lambda_3]$ is constant and equal to q_2.

$\{1, 2 \dots, 311\}$ (0 and 312 are natural and fixed boundaries), i.e. the boundaries are a selection among the hours of the release. Finding the probability distribution of the time steps associated to $\boldsymbol{q}$ is equivalent to finding the probability distribution of Λ. To retrieve the best discretisations of $\boldsymbol{q}$, we can therefore sample Λ.

The RJ-MCMC is basically equivalent to a MH algorithm except that some iterations of the algorithm are not intra-model random jumps (i.e., at constant Λ), but possibly inter-model random jumps (i.e., at non-constant Λ) or transdimensional (i.e., non-constant Λ size).

Specifically, we use three types of random jumps that govern the positions and number of boundaries: birth, death, and move. For these three processes, we draw on the work of Green (1995), Hastie and Green (2012), Liu et al. (2017), and importantly Bodin and Sambridge (2009). The birth process is the creation of a new boundary not present in $\{1, 2, \ldots, 311\}$ yet; the death process is the removal of an existing boundary in Λ, and the move process is the displacement of an existing boundary in Λ. These processes must respect the detailed balance criterion in order to ensure the convergence of the Markov chain to the target distribution (Robert et al., 2018).

3.2 Handling observations and their errors

3.2.1 Measurements fusion

In this subsection, we propose a method to factor both concentration and deposition measurements into a Bayesian sampling by simply taking into account their disparity in the observation error matrix $\mathbf{R}$. First of all, $\mathbf{R}$ is assumed diagonal, hence a collection of scale parameters. Specifically, two scale parameters are used when modelling $\mathbf{R}$: r_c and r_d, associated to the air concentration and deposition measurements, respectively. We can write:

$$\mathbf{R} = \mathrm{diag}(r_c, \ldots, r_c, r_d, \ldots, r_d), \tag{2}$$

where $\mathrm{diag}(\{r_i\}_i)$ is the diagonal matrix of diagonal entries $\{r_i\}_i$. Note that in all subsequent applications, we use the sorting algorithm described by Dumont Le Brazidec et al. (2021) which is applied on both the air concentration and deposition measurements. This algorithm assigns a different scale parameter r_{np} to certain non-pertinent observations to prevent them to reduce artificially r_c and r_d. With this definition of $\mathbf{R}$, the scale variables $r_c, r_d, r_{\mathrm{np}}$ are included in the source vector $\boldsymbol{x}$ and therefore sampled using a MCMC.

3.2.2 Spatio-temporal observation error scale matrix modelling

We propose in this subsection to model $\mathbf{R}$ using the spatio-temporal information of the concentration observations. We assume that the error scale parameter corresponding to an observation-prediction pair depends mainly on the error in the model predictions. It is also proposed to consider a prediction, i.e., an estimation of the amount of radionuclides present at a definite time and place, as a point in a radionuclide plume at a specific time. The prediction modelling error varies according to its spatio-temporal position: spatially, if two points of interest are distant by Δ_x, then the difference of errors in their attached model prediction is empirically assumed to be proportional to Δ_x. Temporally, let us consider two points in a plume with coordinates (x_1, x_2) at times t and $t + \Delta_t$, respectively, where x_1 and x_2 are the longitude and latitude. These two points are moving with the plume, and at time t, they are spatially distant by $v \times \Delta_t$ where v is a reference wind speed, representing the average wind over the accidental period. Therefore the difference of the modelling errors of these points is estimated to be proportional to $\Delta_x = v \times \Delta_t$. In that respect, to each concentration observation y_i can be associated three coordinates:

$$\left(x_{1,i}, x_{2,i}, v \cdot \left(t_i + \frac{\Delta_{t,i}}{2} \right) \right) \tag{3}$$

where $x_{1,i}$, $x_{2,i}$ are the coordinates in km of the observation, v is set equal to $12\,\mathrm{km.h^{-1}}$, t_i and $\Delta_{t,i}$ are the starting time and the duration of the observation in hours. This average wind speed value has not been extensively researched and is only used to estimate the potential of the method. A clustering algorithm such as the k-means algorithm can be applied to partition these three-coordinates observation characteristics in several groups. Then, a scale parameter $r_{c,i}$ can be assigned to each group. If the algorithm for sorting pertinent and non-pertinent observations is applied, this yields

$$\mathbf{R} = \mathrm{diag}(r_{c,i}, r_{\mathrm{np}}, r_{c,j}, \ldots, r_d, r_{\mathrm{np}}) \tag{4}$$

with $r_{c,i}, r_d, r_{\mathrm{np}}$ the scale parameters associated to the spatial or spatio-temporal clusters of air concentration observations, the deposition measurements, and the non-pertinent observations, respectively. The case where only the spatial qualification of the observation is used instead of both the spatial and temporal qualification is also addressed in this study.

4 Application to the Fukushima-Daiichi NPP ^{137}Cs release

In this section we apply the previously introduced methods to the reconstruction of the Fukushima-Daiichi ^{137}Cs source term between 11 and 24 March. But we first define the key statistical assumptions and parameters of the inversion setup.

4.1 Statistical parametrisation

The prior distributions determining the posterior distribution and the transition probabilities of the RJ-MCMC algorithm are defined in the next two sections.

4.1.1 Definition of the prior density functions

In this section, we specify the prior distributions of the source vector components: release rates and hyperparameters. The source release rate logarithms are assumed to follow a folded Gaussian prior distribution, so as to constrain at the same time the number of boundaries and the magnitude of the release rates. In the general case with $\mathrm{N_{imp}} = 312$, the scale matrix $\mathbf{B}$ of the folded Gaussian prior is defined as a 312×312 diagonal matrix. The entry b_k of $\mathbf{B}$ is associated to the k-th hour in $\{0, 1, \ldots, 311\}$, hours where we consider the release of ^{137}Cs possible. This yields:

$$p(\ln \boldsymbol{q} | \mathrm{N_{imp}}) = \prod_{k=0}^{\mathrm{N_{imp}-1}} \sqrt{\frac{2}{\pi b_k}} \left(e^{-\frac{(\ln q_k - \ln q_{\mathrm{b}})^2}{2 b_k}} \right) \tag{5}$$

where the folding position is defined as equal to the location term $\ln q_{\mathrm{b}}$. We divide the 312 time intervals into two groups: the first "unconstrained" group consists of the time intervals during which we have noticed that a radionuclide emission does not trigger any noticeable observation. In other words, it is a time interval during which we have no information on a potential release. The unconstrained time intervals are the first 17 hours of 11 March (hours in $\{0, 1, \ldots, 16\}$), the days of 16 and 17 March (hours in $\{116, 117, \ldots, 165\}$), and the last 18 hours of 23 March (hours in $\{294, 295, \ldots, 311\}$). The second group consists of the constrained time intervals. Two hyperparameters b_{c}, for the constrained time intervals, and b_{nc}, for the unconstrained ones,

are used to describe the matrix $\mathbf{B}$. If, instead of two, a single hyperparameter b is used for all release rates, the unconstrained time intervals are neither regularised by the observations nor by the prior. Indeed, to account for high release rates, samples of the distribution of b reach significant values. Low magnitude release rates are then very little constrained by the corresponding prior. Release rates which are neither constrained by the observations nor by the priors can, in turn, can reach very large values.

205 This phenomenon is put forward by Liu et al. (2017). The mean of the folded Gaussian prior is chosen as $\ln q_{\mathrm{b}} = 0$ in order to regularise the unconstrained intervals. It is important to note that a release rate $\ln q_i$ sampled by the RJ-MCMC is an aggregate of these hourly release rates, each of them associated with either b_c or b_{nc}. We hence define the scale of the prior associated with the release rate $\ln q_i$ defined between times t_i and $t_i + k_i \Delta_t$ as

$$b_i = \frac{\sum_{j=t_i}^{t_i + k_i \Delta_t} \mathbf{B}_{j,j}}{k_i \Delta_t} = \frac{n_{c,i} b_{\mathrm{c}} + (k_i \Delta_t - n_{c,i}) b_{\mathrm{nc}}}{k_i \Delta_t} = w_{\mathrm{c},i} b_{\mathrm{c}} + w_{\mathrm{nc},i} b_{\mathrm{nc}} \tag{6}$$

210 with $\mathbf{B}_{j,j}$ the j-th diagonal coefficient of $\mathbf{B}$, $n_{c,i}$ the portion of constrained time intervals in $k_i \Delta_t$, and with $w_{\mathrm{c},i}$ and $w_{\mathrm{nc},i}$ the weighted numbers of constrained and unconstrained hourly release rates included in the release rate $\ln q_i$. This definition is reflected in the prior cost:

$$\mathbf{J}_{\mathrm{prior}, \ln \boldsymbol{q}} = \sum_{i=0}^{\mathrm{N_{imp}}-1} \left\{ \frac{1}{2} \ln \left(\frac{\pi b_i}{2} \right) + \frac{(\ln q_i)^2}{2 b_i} \right\} \tag{7}$$

$$= \sum_{i=0}^{\mathrm{N_{imp}}-1} \left\{ \frac{1}{2} \ln \left(\frac{\pi (w_{\mathrm{c},i} b_{\mathrm{c}} + w_{\mathrm{nc},i} b_{\mathrm{nc}})}{2} \right) + \frac{(\ln q_i)^2}{2(w_{\mathrm{c},i} b_{\mathrm{c}} + w_{\mathrm{nc},i} b_{\mathrm{nc}})} \right\} \tag{8}$$

215 where $\mathrm{N_{imp}} = \mathrm{N_b} - 1$ is the number of time steps ($\mathrm{N_b}$ being the number of boundaries) considered at a certain iteration by the RJ-MCMC and which characterises the grid on which $\ln \boldsymbol{q}$ is defined. The prior scale parameter b_c is included in the source vector $\boldsymbol{x}$ and sampled with the rest of the variables. Such a prior on the release rate logarithms also has a constraining effect on the model's complexity (Occam's razor principle) through the normalisation constant of the prior pdf.

An exponential prior distribution is used for the boundaries $\Lambda = (\lambda_1, \ldots, \lambda_k)$:

$$220 \quad p(\lambda_1, \ldots, \lambda_k) = \begin{cases} \frac{e^{-k}}{\sum_{i=1}^{\mathrm{N_{b,max}}} \frac{\mathrm{N_{b,max}!}}{i!(\mathrm{N_{b,max}}-i)!} e^{-i}}, & \text{if } k \in \{1, 2, \ldots, \mathrm{N_{b,max}}\}; \\ 0 & \text{otherwise,} \end{cases} \tag{9}$$

with $\mathrm{N_{b,max}} = 311$. This prior has the effect of penalising models that are too complex.

Furthermore, because no a priori information is available, the prior distributions on the coefficients of the observation error scale matrix are assumed to be uniform and the prior on the regularisation scale terms are assumed to follow Jeffreys' prior distribution (Jeffreys, 1946; Liu et al., 2017). The lower and upper bounds of the uniform prior on the coefficients of the

225 observation error matrix are set as 0 and a large value, not necessarily realistic, as in Dumont Le Brazidec et al. (2021).

4.1.2 Parameters of the MCMC algorithm

In the Markov chain, the variables describing the source $\boldsymbol{x}$ are initialised randomly. The intra-model (i.e., with a fixed boundary partition) transitions defining the stochastic walks are set independently for each variable. Each transition probability is defined

as a folded-normal distribution, following Dumont Le Brazidec et al. (2020). Locations of the transition probabilities are the values of the variables at the current step. Variances of the related normal distribution are initialised at $\sigma_{\ln q} = 0.3$, $\sigma_r = 0.01$, the values being chosen by means of experiments. However, the value of σ_r is adaptive and is updated every 1000 iterations according to the predictions values. Furthermore, the value of σ_r is not uniform across groups of observations: there are as many variances as observation clusters.

The algorithm runs initially as a classic MH for 10^4 iterations (only intra-model walks are allowed at this stage). Indeed, allowing transdimensional walks at the beginning of the run sometimes cause Markov chains to get stuck in local minima. In total, 2×10^6 iterations are used which is a large number ensuring the algorithm convergence (i.e. a sufficient sampling of the posterior distribution of $\boldsymbol{x}$) and corresponding to approximately a day of calculation for a 12-core computer. The burn-in is set to 10^6 iterations.

The inter-model transdimensional walks (with changing boundaries) are described in appendix A since it is technical. For this transdimensional case, $u_{\ln q}$ is the same for birth and death processes and is equal to 0.3. There is no variance parameter for the move walk. The probability of proposing an intra-model transition is $1/2$, of proposing a birth transition is $1/6$, of proposing a death transition is $1/6$ and a move transition is $1/6$.

4.2 Results

To evaluate the quality of our reconstructed source term as well as the impact of the techniques proposed in section 3, the distributions of the ^{137}Cs source are sampled and compared under several settings:

- subsection 4.2.1 provides an activity concentration-based reconstruction of the ^{137}Cs source with a log-Cauchy likelihood and a threshold, to ensure it is defined for zero observations or predictions, of $0.5\,\mathrm{Bq.m^{-3}}$ (Dumont Le Brazidec et al., 2021), the application of the observation sorting algorithm, and a spatial representation of $\mathbf{R}$ with 10 parameters. The vector

$$\boldsymbol{x} = \left(\ln \boldsymbol{q}, r_{c,1}, \ldots, r_{c,9}, r_{\mathrm{np}}, b_c, (\lambda_1, \ldots, \lambda_{\mathrm{N_{imp}}-1})\right) \tag{10}$$

is sampled. A log-Cauchy likelihood is chosen because the associated reconstruction produces the best model-to-data comparisons among diverse choices of likelihoods and representations of $\mathbf{R}$. The sampled source is compared to the source terms of Saunier et al. (2013) and Terada et al. (2020) and all variable marginal distributions are described;

- in subsection 4.2.2, we are interested in quantifying the impact of the addition of deposition measurements in the sampling with the method presented in subsection 3.2.1. The source term is sampled in two configurations: with or without the addition of deposition measurements. That is, the vector

$$\boldsymbol{x} = \left(\ln \boldsymbol{q}, r_{c,1}, \ldots, r_{c,9}, r_{\mathrm{np}}, r_d, b_c, (\lambda_1, \ldots, \lambda_{\mathrm{N_{imp}}-1})\right). \tag{11}$$

is sampled with or without r_d. A threshold of $0.5\,\mathrm{Bq.m^{-2}}$ is chosen for the deposition measurements.;

- finally, we draw a selection of violin plots in subsection 4.2.3 to assess the impact of the distribution of the observations in space and time clusters using the approach introduced in subsection 3.2.2. More precisely, the fitness to the observations of the reconstructed source is evaluated given the type of clustering (spatial or spatio-temporal) and the number of clusters.

4.2.1 Best reconstruction and comparison to other source terms

In this section, we provide the most appropriate reconstruction of the source term, based on the activity concentration measurements, from several choices of likelihoods and of $\mathbf{R}$ representations. This best reconstruction is chosen with the help of a model-to-data comparison, i.e., FAC scores, which represent the proportion of measurements for which the observed and modelled values agree. The chosen likelihood is a log-Cauchy distribution with a threshold of $0.5\,\mathrm{Bq.m^{-3}}$ and air concentration measurements are spatially clustered in 9 groups using the k-means method.

Figure 3 shows the temporal evolution of the median release rate with its associated standard deviation, i.e. the evolution of the hourly release rates samples that are obtained from the N_{imp} RJ-MCMC samples. This temporal evolution is compared to the source term from Saunier et al. (2013) which was estimated from gamma dose rate measurements, but from the same meteorological data and transport model, and to the more recent source term from Terada et al. (2020).
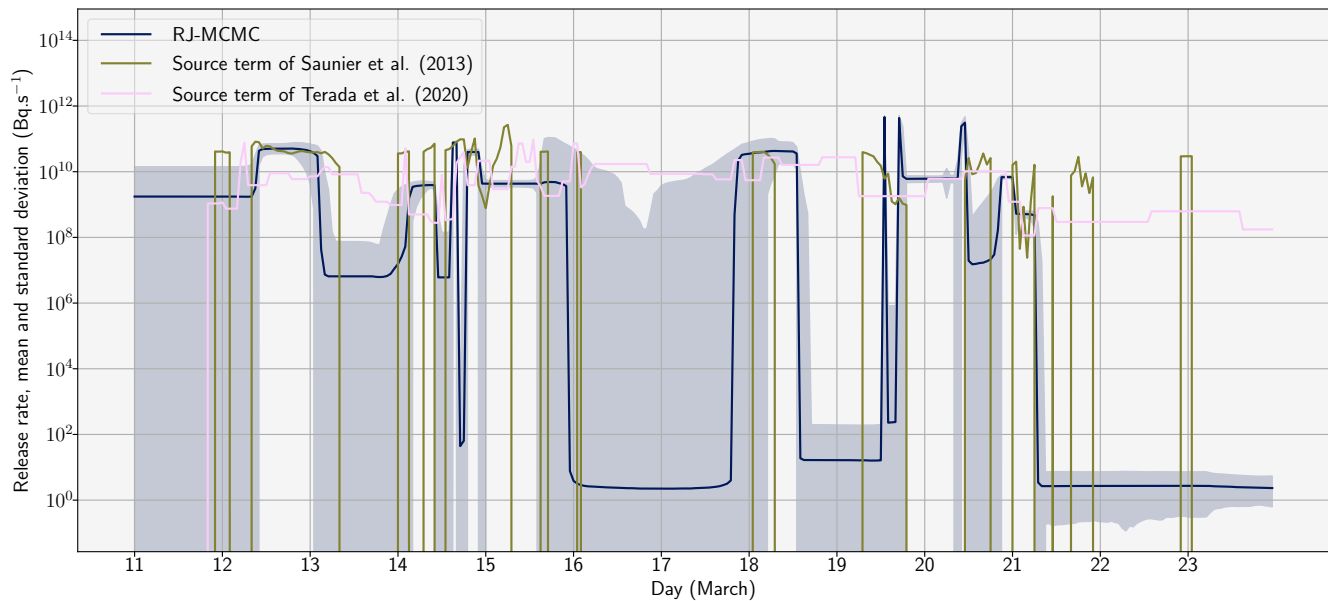

Figure 3. Evolution of the release rate in Bq.s^{-1} describing the ^{137}Cs source (UTC) sampled with the RJ-MCMC algorithm. The blue line corresponds to the sampled median release rate. The light blue area corresponds to the area between $\mu_{\ln q}$ the median and $\sigma_{\ln q}$ the standard deviation of the reconstructed hourly release rates: $[\mu_{\ln q} - \sigma_{\ln q}, \mu_{\ln q} + \sigma_{\ln q}]$. Our source term is compared to the source terms of Saunier et al. (2013) and Terada et al. (2020).

Firstly, we observe that a good match is obtained between the median release and the source term of Saunier et al. (2013) or Terada et al. (2020) (on the constrained time intervals), as the differences between releases under 10^9 Bq.s^{-1} can be neglected.

Indeed, between the 11st and the 19th of March 2011, the three source terms have similar peak magnitudes (close to 10^{11} Bq.s^{-1}); these peaks are observed neighbouring time intervals. Between the 19th and the 21st, a notable difference can be observed: the RJ-MCMC source term predicts very high one-hour peaks (close to 10^{12} Bq.s^{-1}) while the Terada et al. (2020) source term distributes the release uniformly over the whole period. Secondly, release rates are subject to large variations. Indeed, there are periods of important temporal variability of the release rate (e.g., between 19 and 21 March), and of low temporal variability (e.g., between 11 and 14 March). This justifies the use of the RJ-MCMC transdimensional algorithm, as it allows to reconstruct certain time intervals of the release with a greater accuracy and others with a lesser complexity. Thirdly, the temporal evolution of the release can be explored and several prominent peaks can be observed with a magnitude approaching or surpassing 10^{11} Bq.s^{-1}: between 12 and 14 March, between 14 and 16 March, on 18 March, and between 19 and 21 March.

Panel a of Fig. 4 describes the histogram of relative differences in $\log_{10}$ between predictions (medians of the predictions computed using the samples are used) and bigger than 0.5 Bq.m^{-3} air concentration observations. A value of -1 therefore corresponds to an observation 10 times larger than a prediction. A good fit between observations and predictions can be observed although the observations are globally underestimated by the predictions.

Panel b of Fig. 4 shows the pdf of the total release in Bq. It can be seen from this density that most of the total release distribution mass is sampled between 10 and 20 PBq and peaks at 14 PBq. This is consistent with previous studies which estimate the release to be between 5 and 30 PBq (Chino et al., 2011; Terada et al., 2012; Winiarek et al., 2012, 2014; Saunier et al., 2013; Katata et al., 2015; IAEA, 2015; Yumimoto et al., 2016; Liu et al., 2017; Terada et al., 2020). However, note that these works attempt to estimate potential releases beyond 24 March.

Panel c of Fig. 4 plots the pdf of the number of boundaries, i.e. a measure of model complexity, sampled by the algorithm. Here, the minimum of the distribution is 25 boundaries and the maximum is 45 with a peak at 35 boundaries. Recall that the maximum number of boundaries is 313.

Finally, panel d of Fig. 4 shows the average number of sampled boundaries at each time and the associated standard deviation. The y-axis corresponds to the number of boundaries counted: for t a given hour, we draw:

$$\mathrm{E}[\mathrm{Card}\{\lambda_i \in [t-5 \dots t+5] | \lambda_i \in (\lambda_0, \dots, \lambda_{\mathrm{N_{imp}}})\}] \tag{12}$$

i.e. the average over all samples of the number of boundaries counted around t. In essence, the curve shows the number of boundaries necessary to model the release at a certain time, i.e., the variability of the release according to the algorithm. We observe that there is a large variability between 14 and 15 March, and between 19 and 21 March. This correlates very well with the observable results of Fig. 3. This observation confirms once again the relevance of using the RJ-MCMC algorithm: periods of high variability can be sampled finely.
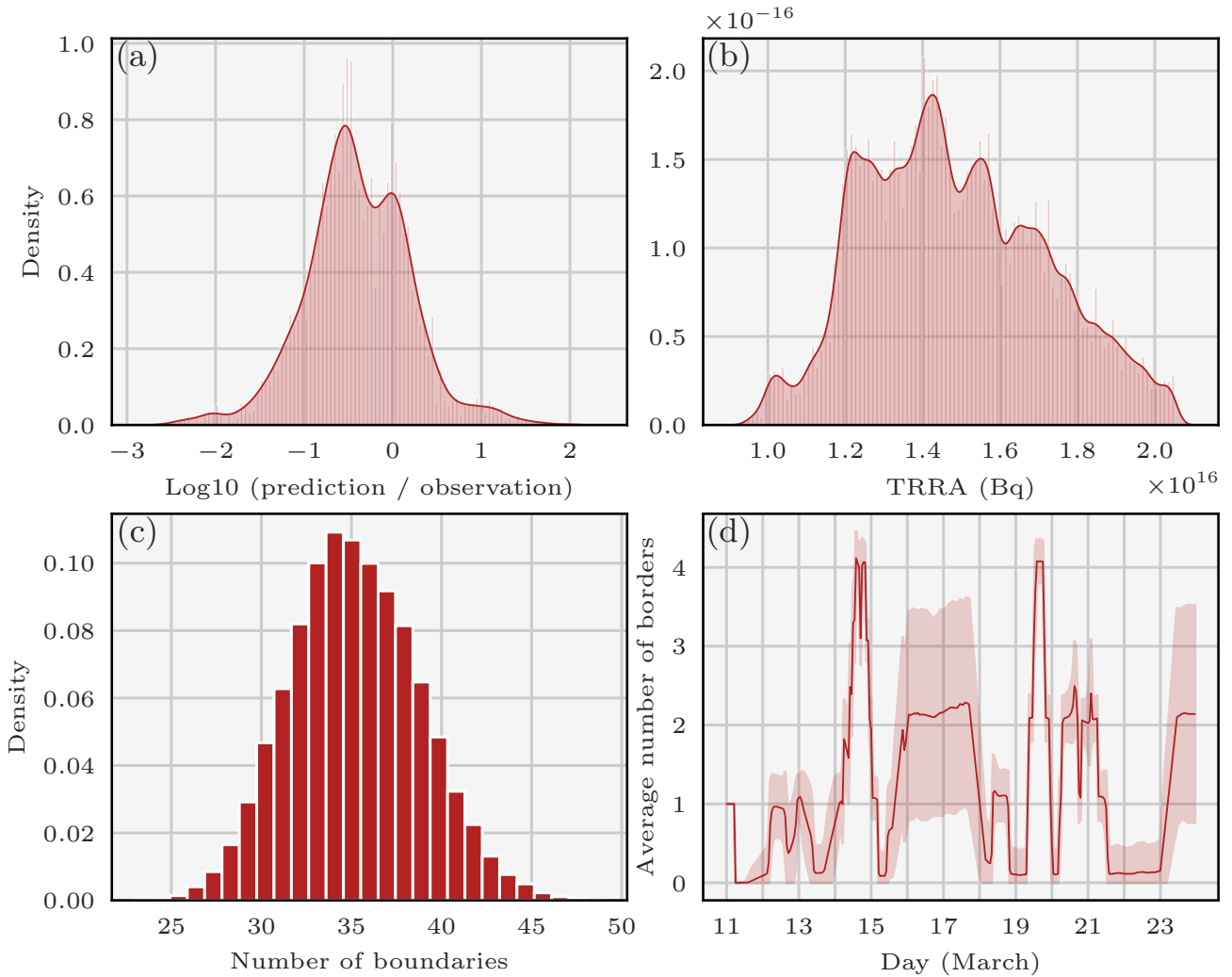
Figure 4. Densities or averages of variables describing the ^{137}Cs source reconstructed with the RJ-MCMC technique.

(a) Density of relative differences in $\log_{10}$ between observations and predictions. (b) Density of the Total Retrieved Released Activity (TRRA) of ^{137}Cs during the Fukushima-Daiichi accident in Bq; outliers are removed. (c) Histogram of the number of boundaries. (d) Mean ($\pm$ standard deviation) of the number of boundaries as a function of time (UTC).

4.2.2 Impact of using deposition measurements

In this section, we study the impact of adding $1,507$ deposition measurements to the $14,248$ air concentration measurements. A log-Cauchy distribution with a threshold of $0.5\,\mathrm{Bq.m^{-3}}$ for the air concentration measurements and $0.5\,\mathrm{Bq.m^{-2}}$ for the deposit measurements is employed. Air concentration measurements are clustered with a spatial k-means algorithm in 9 groups in the same way as described in section 4.2.1. To quantify the impact of the added measurements we sample the following vector with a RJ-MCMC algorithm in two cases, with or without deposition measurements, i.e., with or without r_d:

$$\boldsymbol{x} = \left(\ln \boldsymbol{q}, r_{c,1}, \ldots, r_{c,9}, r_{\mathrm{np}}, r_d, b_c, (\lambda_1, \ldots, \lambda_{\mathrm{N_{imp}}-1}) \right). \tag{13}$$

In the case without deposition measurements, we use the same samples as in subsection 4.2.1. A posteriori marginals of these control variables are displayed in Fig. 5. In Fig. 5.a, the medians of the two samplings are similar, except for the release rates between 11 and 14 March. Indeed, when using air concentration and deposition measurements, the release rate peaks during 12 March instead of 13 March when using air concentrations alone.

In panel b of Fig. 5, the main mode of the TRRA distribution retrieved using the air concentration and deposition measurements is $5\,\mathrm{PBq}$ larger than the TRRA reconstructed with the air concentration measurements alone. Besides, the reconstructed density with both types of measurements has a large variance and leads to the possibility of a larger release (up to $75\,\mathrm{PBq}$). The density of the number of boundaries with both types of measurements is shifted to higher values compared to the density with air concentrations alone, which indicates a reconstructed release of greater complexity (panel c of Fig. 5). This is consistent with the fact that the second release is reconstructed with a larger number of observations.

In panel d of Fig. 5, the number of boundaries was estimated to be half as large on 14 March when deposition measurements were used, but was estimated to be larger on March 15. These differences are rather surprising insofar as there is no obvious disparity between the medians of the release rates for the two reconstructions in panel a of Fig. 5 on these days.

In table 2, we evaluate the FAC 2, FAC 5, FAC 10 scores for both cases. FAC scores are common metrics for measuring the fit of a source term with available observations. The FAC 2, FAC 5, FAC 10 are the proportion of measurements for which the observed and modelled values agree by a factor of 2, 5, or 10, respectively. For example, a FAC 2 score of 0.32 with respect to the air concentration measurements $(y_i)_{i \in \{1, \mathrm{N_{obs}}\}}$ means that $32\,\%$ of the predictions $((\mathbf{Hq})_i)_{i \in \{1, \mathrm{N_{obs}}\}}$ (i.e., simulated measurements) are such that:

$$0.5 < \frac{(\mathbf{Hq})_i + y_t}{y_i + y_t} < 2 \tag{14}$$

with $\mathrm{N_{obs}}$ the number of observations considered, y_t a threshold set at $0.5\,\mathrm{Bq.m^{-3}}$. This threshold is added to limit the weight of low values, considered of lesser interest, in the indicator. Finally, to calculate the FAC scores, only observations above $1\,\mathrm{Bq.m^{-3}}$ are considered.

The FAC scores show that the source term obtained with the RJ-MCMC has a better agreement with the air concentration measurements than the Saunier et al. (2013) or Terada et al. (2020) source term. This shows that the RJ-MCMC is able to sample source terms consistent with air concentration measurements, but does not allow us to conclude on its performance: the sampling algorithm was optimised using air concentrations whereas, for example, the Saunier et al. (2013) source term was
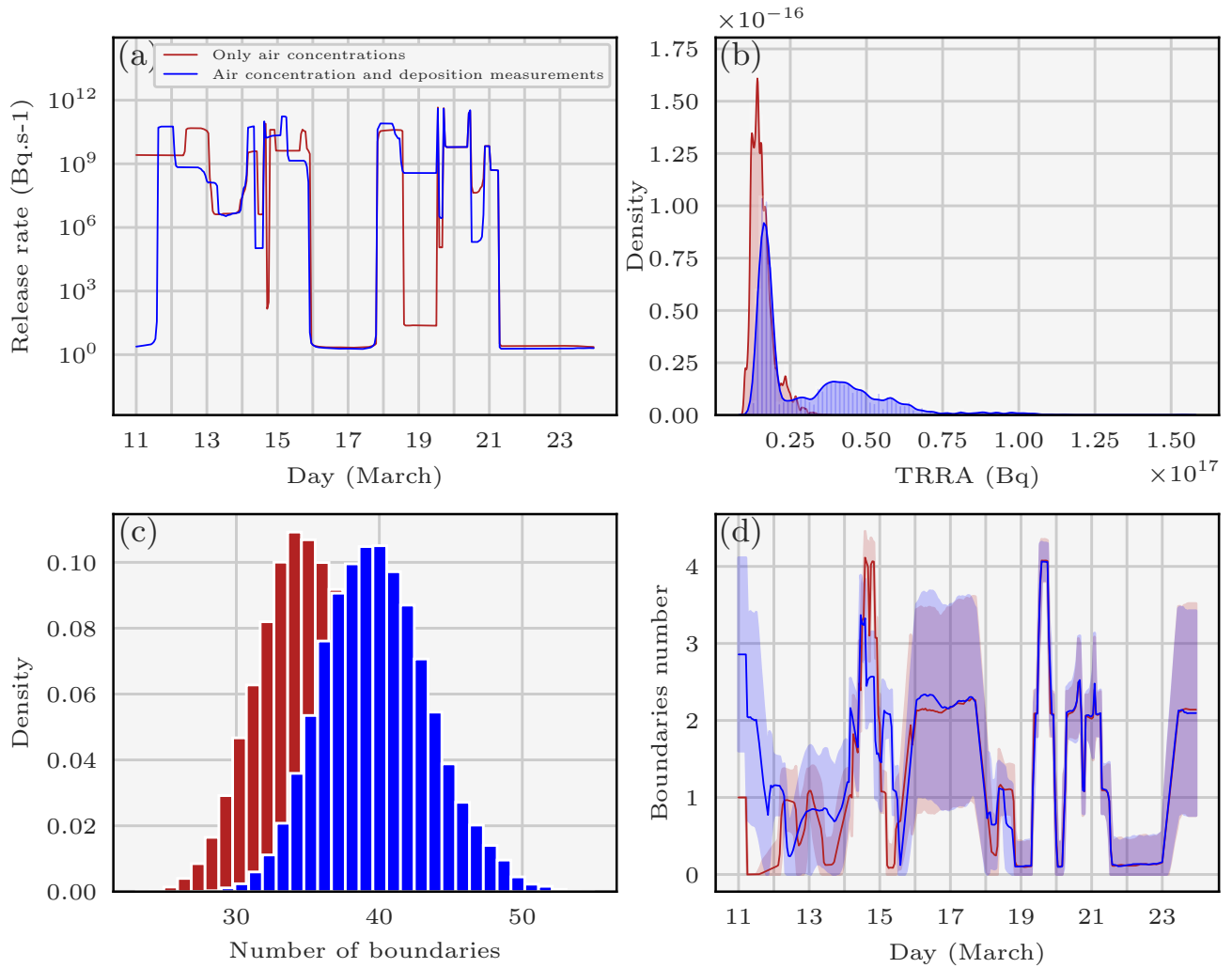
Figure 5. The panels correspond to probability densities or averages of variables describing the ^{137}Cs source reconstructed with the RJ-MCMC technique using air concentration and deposition measurements. (a) Medians and standard deviations of hourly release rates: the red and blue curves correspond to the sampled median release rates. The red and light blue areas correspond to the areas between $\mu_{\ln q}$ the median and $\sigma_{\ln q}$ the standard deviation of the sampled hourly release rates for each reconstruction: $[\mu_{\ln q} - \sigma_{\ln q}, \mu_{\ln q} + \sigma_{\ln q}]$. (b) Probability density of the total release of ^{137}Cs during the Fukushima-Daiichi accident in Bq. (c) Histogram of the number of boundaries. (d) Mean ($\pm$ standard deviation) of the number of boundaries according to the hour considered.

Origin of the source term	FAC 2	FAC 5	FAC 10
RJ-MCMC (based on air concentrations only)			
air concentration	0.32	0.68	0.85
deposition	0.31	0.58	0.75
RJ-MCMC (air concentration and deposition)			
air concentration	0.31	0.67	0.85
deposition	0.49	0.77	0.86
Source term of Saunier et al. (2013)			
air concentration	0.18	0.52	0.76
deposition	0.28	0.64	0.74
Source term of Terada et al. (2020)			
air concentration	0.17	0.52	0.78
deposition	0.29	0.64	0.76

Table 2. Comparison of observed and simulated measurements from reconstructed predictions with air concentration measurements only, or air concentration and deposition measurements. The FAC 2, FAC 5, FAC 10 are the proportion of measurements for which the observed and modelled values agree by a factor of 2, 5, or 10, respectively. The table reads as follows: e.g., the predictions calculated based on air concentrations only, obtain a FAC 5 score of 0.58 with respect to the deposition measurements.

recovered from dose rate measurements. However, the source term found with the RJ-MCMC on air concentration measurements can be fairly evaluated using deposition measurements. It is observed that the fits with the deposition measurements of the three source terms are similar.

Furthermore, as expected, the table shows that there is a significant difference in the fit with the deposition measurements when they are added to the observation dataset used to reconstruct the source term. However, the addition of the deposition measurements has no impact on the quality of the fit to the air concentration measurements. This suggests that a RJ-MCMC optimised on dose rate measurements, in addition to the deposition and air concentrations, may obtain a good agreement with the dose rate measurements, without degrading its results on deposition or air concentrations.

4.2.3 Impact of the observation error matrix $\mathbf{R}$ representation

We investigate in this section the spatial and spatio-temporal representation of the $\mathbf{R}$ likelihood scale matrix. In Fig. 6 are drawn violin plots of the FAC 2 and FAC 5 scores for air concentration measurements against the number of scale parameters chosen to describe $\mathbf{R}$, i.e., the number of observations clusters. Violin plots are created out of the best scores of 44 RJ-MCMC samplings with diverse likelihoods chosen after Dumont Le Brazidec et al. (2021) in order to make the conclusions less

dependent on statistical modelling. The chosen numbers of spatial clusters (1, 2, 9) and spatio-temporal clusters (3, 7) of the violins are a selection for the sake of clarity. It can be observed for both FAC 2 and FAC 5 air concentration scores that the
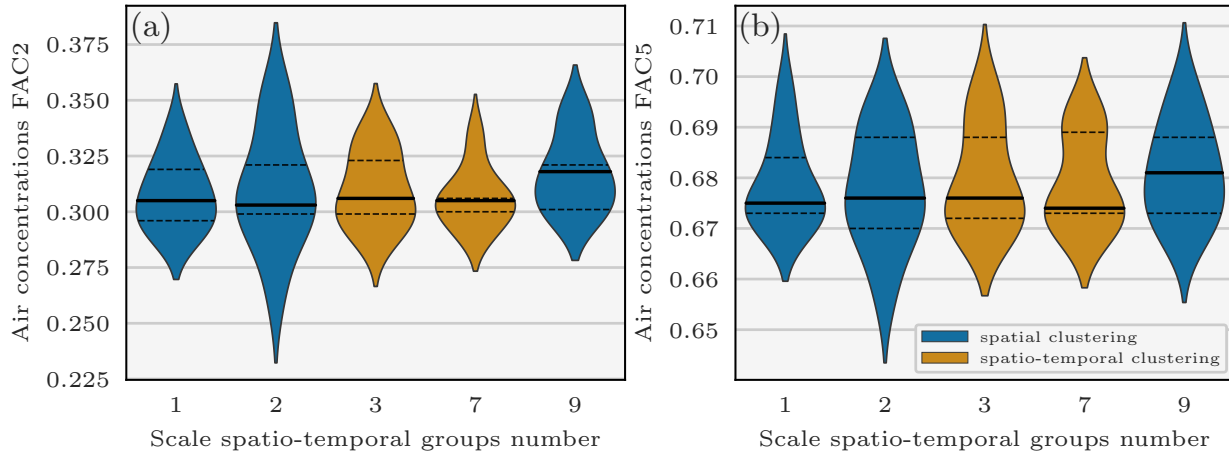

Figure 6. Violin plots of the air concentration FAC 2, FAC 5 scores against the observation error scale parameters spatio-temporal groups number. Points composing the violin plots consist of the best FAC 2, FAC 5 scores of 44 samplings in diverse configurations of likelihoods and thresholds (log-normal, log-Laplace, and log-Cauchy) chosen according to Dumont Le Brazidec et al. (2021). The horizontal segments within the violins represent from bottom to top the first, second and third quartiles, respectively. The chosen numbers of spatial and spatio-temporal clusters are only a selection for the sake of clarity.

spatio-temporal labelling of the observations does not increase the quality of the scores, while the number of spatial clusters does. We can observe for example a difference of 0.02 between the second quartile of the FAC 2 score for samplings with 2 spatial groups and the second quartile of the FAC 2 score for samplings with 9 spatial groups. One hypothesis is that the error is mainly related to the distance to the source and remains relatively homogeneous in time. However, the use of an accurate estimate of the effective wind speed as a function of time and depending on the position of the observations is necessary to draw conclusions; such a study is outside the scope of this paper.

5 Summary and conclusions

In this paper, we investigated a transdimensional sampling method to reconstruct highly fluctuating radionuclide atmospheric sources and applied it to assess the ^{137}Cs Fukushima-Daiichi release. Furthermore we proposed two more methods to add information in the model in order to reduce uncertainties attached to such a complex release.

17

Firstly, a RJ-MCMC algorithm was defined. This MH extension to transdimensional meshes allows to sample both the source term and its underlying adaptive discretisation in time. In the case of complex releases, an adaptive grid allows to reconstruct the source term with high accuracy and discretisation consistent with the available observations.

Secondly, we have focused on ways to add information by adapting the representation of the observation error matrix $\mathbf{R}$. We proposed to assimilate deposition measurements or spatial and temporal information on the air concentration observations by increasing the complexity of $\mathbf{R}$.

Subsequently, the distributions of the variables defining the source of ^{137}Cs were fully sampled. This enabled the estimation of the uncertainties associated with these variables, as well as the evaluation and demonstration of the merits of the methods.

Firstly, we observed that the predictions reproduce well the air concentration and deposition observations. When using air concentrations only, the FAC 2 and FAC 5 scores corresponding to air concentration measurements are 0.32 and 0.68, respectively. The main part of the best total release distribution mass is estimated to be between 10 and $20\,\mathrm{PBq}$ and peaks at $14\,\mathrm{PBq}$ which is in accord with previous estimations.

Secondly, the periods of high variability of ^{137}Cs releases have been reconstructed with accuracy by the RJ-MCMC algorithm. The transdimensional method also allowed the periods of low temporal variability to be sampled more coarsely, thus avoiding variance errors and saving computing time, which, in particular, confirms the conclusions of Liu et al. (2017). The priors we chose allowed for an efficient regularisation of the release rates and their adaptive mesh.

Finally, the use of combined air concentration and deposition measurements had an impact on the reconstruction of the TRRA distribution, the mean of which increased by $10\,\mathrm{PBq}$. The spatial clustering methods proved to increase the quality of the predictions by improving model-to-data comparison.

We recommend the use of the RJ-MCMC for long release source reconstruction. It allows to sample highly variable source terms with great accuracy by solving the bias-variance tradeoff. We also recommend the use of advanced modelling of $\mathbf{R}$ taking in account the deposition measurements and the spatial information of the air concentration observations which have proven to be valuable in reducing the observation-prediction discrepancies.

Appendix A: RJ-MCMC mathematical details

We describe here the mathematical details of the three inter-model walks: move, birth and death. The move process is intra-dimensional. Provided that the move is a symmetric motion, the associated g-transition distribution is symmetric, i.e.:

$$\frac{g(\boldsymbol{x}_i|\boldsymbol{x}_j)}{g(\boldsymbol{x}_j|\boldsymbol{x}_i)} = 1. \tag{A1}$$

The birth process is the creation of a new boundary, a walk from $\boldsymbol{x}_i$ a vector composed of n boundaries to $\boldsymbol{x}_j$ a vector composed of $n+1$ boundaries is proposed. In other words, by generating a new boundary, one release rate is destroyed and two new release rates emerge from this destruction. We therefore assign two new release rates $\ln q'_{k-1} = \ln q_{k-1} - u_{\ln q}$ and $\ln q'_k = \ln q_{k-1} + u_{\ln q}$ with $u_{\ln q}$ a Gaussian noise. The transition probability is defined as follows (Bodin and Sambridge,

2009):

$$g(\Lambda_i, \ln \boldsymbol{q}_i | \Lambda_j, \ln \boldsymbol{q}_j) = g(\Lambda_i | \Lambda_j, \ln \boldsymbol{q}_j) \, g(\ln \boldsymbol{q}_i | \Lambda_i, \Lambda_j, \ln \boldsymbol{q}_j) = g(\Lambda_i | \Lambda_j) \, g(\ln \boldsymbol{q}_i | \ln \boldsymbol{q}_j, \Lambda_i). \tag{A2}$$

The probability of a birth at a certain position among $N_{b,max} - N_{imp} + 1$ positions not occupied by boundaries is

$$g(\Lambda_i | \Lambda_j) = \frac{1}{N_{b,max} - N_{imp} + 1}. \tag{A3}$$

Furthermore, the probability of generating new release rates is Gaussian:

$$g(\ln \boldsymbol{q}_i | \Lambda_i, \ln \boldsymbol{q}_j) = g(\ln q'_{k-1}, \ln q'_k | \ln q_{k-1}, u_{\ln q}) = \frac{1}{\sqrt{2\pi}\sigma} e^{-\frac{u_{\ln q}^2}{2\sigma^2}}, \tag{A4}$$

where the new boundary is here generated at hour $k - 1$.

The probability of death of one among the $N_{imp} - 1$ boundaries is

$$g(\Lambda_j | \Lambda_i) = \frac{1}{N_{imp} - 1}, \tag{A5}$$

which is a uniform choice among $N_{imp} - 1$ possibilities. On the other hand, the probability $g(\ln \boldsymbol{q}_j | \Lambda_j, \Lambda_i, \ln \boldsymbol{q}_i)$ of destroying the release associated to this position is 1.

Author contributions. Joffrey Dumont Le Brazidec: Software, Methodology, Conceptualisation, Investigation, Writing - Original Draft, Visualisation. Marc Bocquet: Methodology, Software, Conceptualisation, Writing - Review and Editing, Visualisation, Supervision. Olivier Saunier: Resources, Methodology, Conceptualisation, Writing - Review and Editing, Visualisation, Supervision. Yelva Roustan: Methodology, Software, Writing - Review and Editing.

19

References

Baklanov, A. and Sørensen, J. H.: Parameterisation of radionuclide deposition in atmospheric long-range transport modelling, Phys Chem Earth, Part B: Hydrology, Oceans and Atmosphere, 26, 787–799, https://doi.org/10.1016/S1464-1909(01)00087-9, 2001.

Bodin, T. and Sambridge, M.: Seismic tomography with the reversible jump algorithm, Geophys. J. Int., 178, 1411–1436, https://doi.org/10.1111/j.1365-246X.2009.04226.x, 2009.

Chino, M., Nakayama, H., Nagai, H., Terada, H., Katata, G., and Yamazawa, H.: Preliminary Estimation of Release Amounts of 131I and 137Cs Accidentally Discharged from the Fukushima Daiichi Nuclear Power Plant into the Atmosphere, J Nucl Sci Technol, 48, 1129–1134, https://doi.org/10.1080/18811248.2011.9711799, 2011.

Delle Monache, L., Lundquist, J., Kosović, B., Johannesson, G., Dyer, K., Aines, R. D., Chow, F., Belles, R., Hanley, W., Larsen, S., Loosmore, G., Nitao, J., Sugiyama, G., and Vogt, P.: Bayesian inference and markov chain monte carlo sampling to reconstruct a contaminant source on a continental scale, J. Appl. Meteorol. Climatol., 47, 2600–2613, https://doi.org/10.1175/2008JAMC1766.1, 2008.

Dumont Le Brazidec, J., Bocquet, M., Saunier, O., and Roustan, Y.: MCMC methods applied to the reconstruction of the autumn 2017 Ruthenium-106 atmospheric contamination source, Atmos. Environ., 6, 100 071, https://doi.org/10.1016/j.aeaoa.2020.100071, 2020.

Dumont Le Brazidec, J., Bocquet, M., Saunier, O., and Roustan, Y.: Quantification of the modelling uncertainties in atmospheric release source assessment and application to the reconstruction of the autumn 2017 Ruthenium 106 source, Atmos. Chem. Phys., pp. 1–28, https://doi.org/10.5194/acp-2020-1129, publisher: Copernicus GmbH, 2021.

Furuta, S., Sumiya, S., Watanabe, H., Nakano, M., Imaizumi, K., Takeyasu, M., Nakada, A., Fujita, H., Mizutani, T., Morisawa, M., Kokubun, Y., Kono, T., Nagaoka, M., Yokoyama, H., Hokama, T., Isozaki, T., Nemoto, M., Hiyama, Y., Onuma, T., Kato, C., and Kurachi, T.: Results of the environmental radiation monitoring following the accident at the Fukushima Daiichi Nuclear Power Plant Interim report Ambient radiation dose rate, radioactivity concentration in the air and radioactivity concentration in the fallout, Tech. rep., Radiation Protection Department, Nuclear Fuel Cycle Engineering Laboratories, Tokai Research and Development Center, Japan Atomic Energy Agency, Japan, jAEA-Review–2011-035 INIS Reference Number: 43088311, 2011.

Green, P. J.: Reversible jump Markov chain Monte Carlo computation and Bayesian model determination, Biometrika, 82, 711–732, https://doi.org/10.1093/biomet/82.4.711, 1995.

Hastie, D. I. and Green, P. J.: Model choice using reversible jump Markov chain Monte Carlo, Stat. Neerl., 66, 309–338, https://doi.org/10.1111/j.1467-9574.2012.00516.x, 2012.

Hastie, T., Tibshirani, R., and Friedman, J.: The Elements of Statistical Learning: Data Mining, Inference, and Prediction, Second Edition, Springer Series in Statistics, Springer-Verlag, New York, 2 edn., 2009.

Hirao, S., Yamazawa, H., and Nagae, T.: Estimation of release rate of iodine-131 and cesium-137 from the Fukushima Daiichi nuclear power plant, J Nucl Sci Technol, 50, 139–147, https://doi.org/10.1080/00223131.2013.757454, 2013.

IAEA: The Fukushima Daiichi accident, Tech. rep., Vienna, 2015.

Jeffreys, H.: An invariant form for the prior probability in estimation problems, Proceedings of the Royal Society of London. Series A. Mathematical and Physical Sciences, 186, 453–461, https://doi.org/10.1098/rspa.1946.0056, publisher: Royal Society, 1946.

Katata, G., Ota, M., Terada, H., Chino, M., and Nagai, H.: Atmospheric discharge and dispersion of radionuclides during the Fukushima Daiichi Nuclear Power Plant accident. Part I: Source term estimation and local-scale atmospheric dispersion in early phase of the accident, J. Environ. Radioact., 109, 103–113, https://doi.org/10.1016/j.jenvrad.2012.02.006, 2012.

Katata, G., Chino, M., Kobayashi, T., Terada, H., Ota, M., Nagai, H., Kajino, M., Draxler, R., Hort, M. C., Malo, A., Torii, T., and Sanada, Y.: Detailed source term estimation of the atmospheric release for the Fukushima Daiichi Nuclear Power Station accident by coupling simulations of an atmospheric dispersion model with an improved deposition scheme and oceanic dispersion model, Atmos. Chem. Phys., 15, 1029–1070, https://doi.org/10.5194/acp-15-1029-2015, publisher: Copernicus GmbH, 2015.

460 Keats, A., Yee, E., and Lien, F.-S.: Bayesian inference for source determination with applications to a complex urban environment, Atmos. Environ., 41, 465–479, https://doi.org/10.1016/j.atmosenv.2006.08.044, 2007.

Kobayashi, T., Nagai, H., Chino, M., and Kawamura, H.: Source term estimation of atmospheric release due to the Fukushima Dai-ichi Nuclear Power Plant accident by atmospheric and oceanic dispersion simulations, J Nucl Sci Technol, 50, 255–264, https://doi.org/10.1080/00223131.2013.772449, publisher: Taylor & Francis _eprint: https://doi.org/10.1080/00223131.2013.772449,
465 2013.

Li, X., Sun, S., Hu, X., Huang, H., Li, H., Morino, Y., Wang, S., Yang, X., Shi, J., and Fang, S.: Source inversion of both long- and short-lived radionuclide releases from the Fukushima Daiichi nuclear accident using on-site gamma dose rates, J. Hazard. Mater., 379, 120 770, https://doi.org/10.1016/j.jhazmat.2019.120770, 2019.

Liu, Y., Haussaire, J.-M., Bocquet, M., Roustan, Y., Saunier, O., and Mathieu, A.: Uncertainty quantification of pollutant source retrieval:
470 comparison of Bayesian methods with application to the Chernobyl and Fukushima Daiichi accidental releases of radionuclides, Q. J. R. Meteorol. Soc., 143, 2886–2901, https://doi.org/10.1002/qj.3138, 2017.

Louis, J.-F.: A parametric model of vertical eddy fluxes in the atmosphere, Boundary Layer Meteorol, 17, 187–202, https://doi.org/10.1007/BF00117978, 1979.

Mathieu, A., Korsakissok, I., Quélo, D., Groëll, J., Tombette, M., Didier, D., Quentric, E., Saunier, O., Benoit, J.-P., and Isnard, O.: Atmo-
475 spheric Dispersion and Deposition of Radionuclides from the Fukushima Daiichi Nuclear Power Plant Accident, Elements, 8, 195–200, https://doi.org/10.2113/gselements.8.3.195, publisher: GeoScienceWorld, 2012.

MEXT: NRA: Results of the (i) Fifth Airborne Monitoring Survey and (ii) Airborne Monitoring Survey Outside 80 km from the Fukushima Dai-ichi NPP, http://radioactivity.nsr.go.jp/en/contents/6000/5790/24/203_0928_14e.pdf, 2012.

Nagai, H., Terada, H., Tsuduki, K., Katata, G., Ota, M., Furuno, A., and Akari, S.: Updating source term and atmospheric disper-
480 sion simulations for the dose reconstruction in Fukushima Daiichi Nuclear Power Station Accident, EPJ Web Conf., 153, 08 012, https://doi.org/10.1051/epjconf/201715308012, publisher: EDP Sciences, 2017.

Nagakawa, Y., Sotodate, T., Kinjo, Y., and Suzuki, T.: One-year time variations of anthropogenic radionuclides in aerosols in Tokyo after the Fukushima Dai-ichi Nuclear Power Plant reactor failures, J Nucl Sci Technol, 52, https://doi.org/10.1080/00223131.2014.985279, 2015.

Oura, Y., Ebihara, M., Tsuruta, H., Nakajima, T., Ohara, T., Ishimoto, M., Sawahata, H., Katsumura, Y., and Nitta, W.: A Database of
485 Hourly Atmospheric Concentrations of Radiocesium (^{134}Cs and ^{137}Cs) in Suspended Particulate Matter Collected in March 2011 at 99 Air Pollution Monitoring Stations in Eastern Japan, J. Nucl. Radiochem. Sci., 15, 2_1–2_12, https://doi.org/10.14494/jnrs.15.2_1, 2015.

Querel, A., Quelo, D., Roustan, Y., and Mathieu, A.: Sensitivity study to select the wet deposition scheme in an operational atmospheric transport model, Journal of Environmental Radioactivity, 237, 106 712, https://doi.org/10.1016/j.jenvrad.2021.106712, publisher: Elsevier, 2021.

490 Quélo, D., Krysta, M., Bocquet, M., Isnard, O., Minier, Y., and Sportisse, B.: Validation of the Polyphemus platform on the ETEX, Chernobyl and Algeciras cases, Atmos. Environ., 41, 5300–5315, https://doi.org/10.1016/j.atmosenv.2007.02.035, 2007.

Robert, C. P., Elvira, V., Tawn, N., and Wu, C.: Accelerating MCMC algorithms, Wiley Interdiscip. Rev. Comput. Stat., 10, e1435, https://doi.org/10.1002/wics.1435, 2018.

Saunier, O., Mathieu, A., Didier, D., Tombette, M., Quélo, D., Winiarek, V., and Bocquet, M.: An inverse modeling method to assess the
source term of the Fukushima Nuclear Power Plant accident using gamma dose rate observations, Atmos. Chem. Phys., 13, 11 403–11 421,
https://doi.org/10.5194/acp-13-11403-2013, 2013.

Saunier, O., Didier, D., Mathieu, A., Masson, O., and Dumont Le Brazidec, J.: Atmospheric modeling and source reconstruc-
tion of radioactive ruthenium from an undeclared major release in 2017, Proc. Natl. Acad. Sci. U.S.A., 116, 24 991–25 000,
https://doi.org/10.1073/pnas.1907823116, 2019.

Stohl, A., Seibert, P., Wotawa, G., Arnold, D., Burkhart, J. F., Eckhardt, S., Tapia, C., Vargas, A., and Yasunari, T. J.: Xenon-133 and
caesium-137 releases into the atmosphere from the Fukushima Dai-ichi nuclear power plant: determination of the source term, atmospheric
dispersion, and deposition, Atmos. Chem. Phys., 12, 2313–2343, https://doi.org/10.5194/acp-12-2313-2012, 2012.

Takehisa, O., Tetsuya, O., Mitsumasa, T., Yukio, S., Masamitsu, K., Hitoshi, A., Yasuaki, K., Masatsugu, K., Jun, S., Masahiro, T., Hitoshi,
O., Shunsuke, T., Shunsuke, T., Tadahiro, S., and Tadahiro, S.: Emergency Monitoring of Environmental Radiation and Atmospheric
Radionuclides at Nuclear Science Research Institute, JAEA Following the Accident of Fukushima Daiichi Nuclear Power Plant, JAEA-
Data, https://jglobal.jst.go.jp/en/detail?JGLOBAL_ID=201402276577269847, 2012.

Tanaka, K., Sakaguchi, A., Kanai, Y., Tsuruta, H., Shinohara, A., and Takahashi, Y.: Heterogeneous distribution of radiocesium in aerosols,
soil and particulate matters emitted by the Fukushima Daiichi Nuclear Power Plant accident: retention of micro-scale heterogeneity during
the migration of radiocesium from the air into ground and river systems, Journal of Radioanalytical and Nuclear Chemistry, 295, 1927–
1937, https://doi.org/10.1007/s10967-012-2160-9, 2013.

Terada, H., Katata, G., Chino, M., and Nagai, H.: Atmospheric discharge and dispersion of radionuclides during the Fukushima Dai-ichi
Nuclear Power Plant accident. Part II: verification of the source term and analysis of regional-scale atmospheric dispersion, J. Environ.
Radioact., 112, 141–154, https://doi.org/10.1016/j.jenvrad.2012.05.023, 2012.

Terada, H., Nagai, H., Tsuduki, K., Furuno, A., Kadowaki, M., and Kakefuda, T.: Refinement of source term and atmospheric disper-
sion simulations of radionuclides during the Fukushima Daiichi Nuclear Power Station accident, J. Environ. Radioact., 213, 106 104,
https://doi.org/10.1016/j.jenvrad.2019.106104, 2020.

Tichý, O., Šmídl, V., Hofman, R., and Stohl, A.: LS-APC v1.0: a tuning-free method for the linear inverse problem and its application to
source-term determination, Geosci. Model Dev., 9, 4297–4311, https://doi.org/10.5194/gmd-9-4297-2016, 2016.

Troen, I. B. and Mahrt, L.: A simple model of the atmospheric boundary layer; sensitivity to surface evaporation, Bound.-Layer Meteorol.,
37, 129–148, https://doi.org/10.1007/BF00122760, 1986.

Tsuruta, H., Oura, Y., Ebihara, M., Moriguchi, Y., Ohara, T., and Nakajima, T.: Time-series analysis of atmospheric radiocesium at two SPM
monitoring sites near the Fukushima Daiichi Nuclear Power Plant just after the Fukushima accident on March 11, 2011, Geochemical
Journal, 52, 103–121, https://doi.org/10.2343/geochemj.2.0520, 2018.

Winiarek, V., Bocquet, M., Saunier, O., and Mathieu, A.: Estimation of errors in the inverse modeling of accidental release of atmospheric
pollutant: Application to the reconstruction of the cesium-137 and iodine-131 source terms from the Fukushima Daiichi power plant, J.
Geophys. Res. (Atmospheres), 117, D05 122, https://doi.org/10.1029/2011JD016932, 2012.

Winiarek, V., Bocquet, M., Duhanyan, N., Roustan, Y., Saunier, O., and Mathieu, A.: Estimation of the caesium-137 source term from the
Fukushima Daiichi nuclear power plant using a consistent joint assimilation of air concentration and deposition observations, Atmos.
Environ., 82, 268–279, https://doi.org/10.1016/j.atmosenv.2013.10.017, 2014.

Yamada, J., Seya, N., Haba, R., Muto, Y., Shimizu, T., Takasaki, K., Numari, H., Sato, N., Nemoto, K., and Takasaki, H.: Environmen-
tal radiation monitoring resulting from the accident at the Fukushima Daiichi Nuclear Power Plant, conducted by Oarai Research and

Development Center, JAEA Results of ambient gamma-ray dose rate, atmospheric radioactivity and meteorological observation, Tech. Rep. Code–2013-006 INIS Reference Number: 48050473, Oarai Research and Development Center, Japan Atomic Energy Agency (In Japanese), Japan, 2013.

535   Yee, E.: Theory for Reconstruction of an Unknown Number of Contaminant Sources using Probabilistic Inference, Boundary-Layer Meteorology, 127, 359–394, https://doi.org/10.1007/s10546-008-9270-5, 2008.

Yee, E., Hoffman, I., and Ungar, K.: Bayesian Inference for Source Reconstruction: A Real-World Application, Int Sch Res Notices, 2014, https://doi.org/10.1155/2014/507634, 2014.

Yumimoto, K., Morino, Y., Ohara, T., Oura, Y., Ebihara, M., Tsuruta, H., and Nakajima, T.: Inverse modeling of the 137Cs source term of

540   the Fukushima Dai-ichi Nuclear Power Plant accident constrained by a deposition map monitored by aircraft, J. Environ. Radioact., 164, 1–12, https://doi.org/10.1016/j.jenvrad.2016.06.018, 2016.